ARTICLE

CrossMark

Timing and genesis of Cu–(Au) mineralization in the Khetri Copper Belt, northwestern India: constraints from in situ U–Pb ages and Sm–Nd isotopes of monazite-(Ce)

Xiao-Chun Li[1] · Mei-Fu Zhou[1] · A. E. Williams-Jones[2] · Yue-Heng Yang[3] · Jian-Feng Gao[4]

© Springer-Verlag GmbH Germany, part of Springer Nature 2018

Abstract

The Khetri Copper Belt (KCB) in northwestern India contains several economically important hydrothermal Cu–(Au) deposits. Orebodies in these deposits are locally rich in monazite-(Ce). In this study, in situ U–Pb ages and Sm–Nd isotopic compositions of monazite-(Ce) are used to constrain the timing of mineralization and to better understand the genesis of the Cu–(Au) deposits. Monazite-(Ce) crystals were identified in the Madhan-Kudhan and Kolihan deposits in the KCB. Most monazite-(Ce) crystals in the two deposits show close textural associations with hydrothermal minerals (biotite, chlorite, and sulfide) and have low contents of ThO_2 (mostly < 2 wt.%), indicating a hydrothermal origin. The hydrothermal monazite-(Ce) crystals have U–Pb ages of 833 ± 5 to 840 ± 6 Ma, which are interpreted to represent the timing of the mineralization in the KCB. Another set of monazite-(Ce) crystals in the Kolihan deposit has relatively high contents of ThO_2 (4.72 wt.% on average) and commonly shows concentric zonation with respect to Th. They have a weighted average $^{207}Pb/^{206}Pb$ age of 1362 ± 29 Ma, which may record a pre-ore metamorphic event in the KCB. Hydrothermal monazite-(Ce) crystals from the Madhan-Kudhan deposit have $\varepsilon_{Nd}(t = 835$ Ma) values ranging from -4.3 to -16.8 (-9.6 on average), indicating that isotopically heterogeneous materials were in the metal sources or along the flow paths of hydrothermal fluids. The ages of Cu–(Au) deposits in the KCB fall within the age range of the regional Ca–Na metasomatism (~ 830 to ~ 850 Ma). Combining this temporal association with relevant geochemical and isotopic data, we propose that circulation of hydrothermal fluids caused widespread Ca–Na metasomatism, mobilized certain ore-metals, and thus facilitated the formation of Cu–(Au) deposits.

Keywords Monazite–(Ce) · U–Pb dating · Sm–Nd isotopes · Neoproterozoic · Khetri Copper Belt

✉ Xiao-Chun Li
lixiaochun86@gmail.com

✉ Mei-Fu Zhou
mfzhou@hku.hk

[1] Department of Earth Sciences, The University of Hong Kong, Pokfulam, Hong Kong SAR, China

[2] Department of Earth and Planetary Sciences, McGill University, Montreal, Canada

[3] State Key Laboratory of Lithospheric Evolution, Institute of Geology and Geophysics, Chinese Academy of Sciences, Beijing, China

[4] State Key Laboratory of Ore Deposit Geochemistry, Institute of Geochemistry, Chinese Academy of Sciences, Guiyang, China

Introduction

Several $Cu \pm Au \pm Fe \pm REE \pm U$ deposits are hosted in Proterozoic metasedimentary rocks of the Aravalli–Delhi Fold Belt, northwestern India, which is referred as the Khetri Copper Belt (KCB). These deposits contain ~ 140 Mt ore at 1.1 to 1.7 wt.% Cu and 0.5 g/t Au, making the KCB one of the largest Cu metallogenic provinces in India (Knight et al. 2002). An early model proposed a syngenetic origin for the deposits, in which the ore was suggested to form during sedimentation or diagenesis and was subsequently metamorphosed (Sarkar and Dasgupta 1980). Another model considered that the mineralization formed epigenetically and was genetically associated with regional magmatism (Das Gupta 1974). Recent studies, however, have emphasized the Iron Oxide–Copper–Gold (IOCG)-like affinity of the deposits (Knight et al. 2002; Kaur et al. 2014; Baidya et al. 2017).

Establishing the timing of mineralization is important for understanding the ore genesis. A mean fission track age of 897 ± 125 Ma was reported for garnet from the Madhan-Kudhan deposit in the KCB and was thought to represent the timing of Cu–(Au) mineralization (Knight et al. 2002). However, garnet is a metamorphic mineral rather than a hydrothermal mineral in the Madhan-Kudhan deposit. Thus, the fission track age cannot be taken as the age of ore formation. Moreover, the large uncertainty in the age determination makes it of questionable use even in constraining the age of the metamorphism. In order to properly constrain the ore-forming age, it is necessary to date ore-related minerals and to use robust isotopic methods that can yield reliable ages. It is well-known that monazite can form from hydrothermal fluids, and it has been reported in many hydrothermal deposit types (e.g., VMS-type deposits, Davis et al. 1994; Sn-porphyry deposits, Kempe et al. 2008; orogenic gold deposits, Rasmussen et al. 2006; magmatic-hydrothermal REE deposits, Pandur et al. 2016; and IOCG deposits, Li et al. 2018). Hydrothermal monazite commonly contains high U and/or Th, but negligible common Pb and its U–Th–Pb system have closure temperatures greater than 700 °C (Williams et al. 2007; Chiaradia et al. 2013). Thus, it has characteristics useful for determining the age of hydrothermal deposits.

Monazite has high concentrations of Sm and Nd, which permits submineral-scale determination of Sm–Nd isotopic compositions (Fisher et al. 2011; Liu et al. 2012; Goudie et al. 2014). Importantly, such micro-scale analyses may reveal isotopic heterogeneities within and between single grains (Gregory et al. 2009a; Fisher et al. 2017), which were obscured by conventional whole-rock isotopic analysis.

In this study, we present textural features and compositions of monazite-(Ce) from two representative deposits in the KCB and demonstrate that monazite-(Ce) is a hydrothermal mineral. In situ U–Pb dating on hydrothermal monazite-(Ce) places constraints on the timing of the mineralization. In addition, in situ Sm–Nd isotopic compositions of hydrothermal monazite-(Ce) and bulk-rock Sm–Nd isotopic compositions of ore-hosting metasedimentary rocks are used to trace the source(s) of REE in the ore. The new dataset allows us to better understand the origin of the Cu–(Au) deposits in the KCB.

Regional geology

The Aravalli–Delhi Fold Belt represents a major NE–SW tectonic lineament in the northwestern part of the Indian subcontinent (Fig. 1a). The oldest rock unit of this belt is the Banded Gneissic Complex (BGC), which has been divided into two disconnected units, namely BGC-I and BGC-II (Fig. 1b; Heron 1953). The BGC-I unit contains Archean (~ 3.3 Ga) tonalite–trondhjemite–granodiorite (TTG) gneiss that was intruded by 2.8–2.5 Ga granitoids (Wiedenbeck and Goswami 1994; Roy and Kröner 1996; Wiedenbeck et al. 1996). The BGC-II unit comprises Archean gneiss (2.9 to 2.5 Ga; Dharma Rao et al. 2011; Roy et al. 2012), intruded by granitic magmas at 1.73–1.72 Ga and metamorphosed at ca. 1.85, 1.73, 1.62, and 1.0–0.95 Ga (Roy et al. 2005; Buick et al. 2006, 2010; Bhowmik et al. 2010; Hazarika et al. 2013).

The BGC is in tectonic contact with, or unconformably overlain by, two Proterozoic supracrustal sequences, the Aravalli and Delhi Supergroups. The Aravalli Supergroup is widely distributed in the eastern and southeastern segments of the Aravalli–Delhi Fold Belt along a NE–SW trending basin (Fig. 1b). It consists mainly of greenschist- to amphibolite-facies siliciclastic rocks and carbonates, with local mafic volcanic rocks, phosphorites, and VMS-type Pb–Zn deposits (Sinha-Roy et al. 1998). Geochronological studies showed that Aravalli sedimentation spanned the time interval from ~ 2.3 to ~ 1.6 Ga (Ahmad et al. 2008; McKenzie et al. 2013).

The Delhi Supergroup has been divided into two belts, namely the North and South Delhi Fold Belts (Fig. 1b). The North Delhi Fold Belt hosts a succession of greenschist to amphibolite-facies metasediments, comprising the quartzite-dominated Alwar Group and the schist-dominated Ajabgarh Group. The sedimentary successions were deposited after 1.71 Ga (Kaur et al. 2011a). The South Delhi Fold Belt consists of quartzite, schist, metaconglomerate, carbonate, and minor metavolcanic rocks, which have been tightly folded into a regional synclinorium and metamorphosed up to amphibolite facies (Heron 1953; Gupta et al. 1998). The depositional age of the South Delhi Fold Belt sediments is estimated at 1.2 to 1.0 Ga (McKenzie et al. 2013).

Closure of the Delhi basin was marked by the ~ 1.0 to ~ 0.9 Ga collision between the Marwar Craton in the west and the Bundelkhand Craton in the east (Vijaya Rao et al. 2000; Bhowmik et al. 2010; Fig. 1a). This collision event is marked by metamorphism in the central and northern domains of the Aravalli–Delhi Fold Belt (Pant et al. 2008; Bhowmik et al. 2010; Hazarika et al. 2013; Ozha et al. 2016) and local magmatism in the southern domain of this fold belt (Deb et al. 2001; Pandit et al. 2003, 2011).

A suite of Neoproterozoic (~ 870 to ~ 800 Ma) granitic intrusions, termed Erinpura Granites, occurs widely in the southern segment of the Aravalli–Delhi Fold Belt (Fig. 1b; Deb et al. 2001; Van Lente et al. 2009; Just et al. 2011). The Erinpura Granites include variably deformed felsic intrusions composed of granite, tonalite, diorite, and granitic gneisses. Northwest of the Erinpura Granites is the ~ 770 to ~ 750 Ma Malani Igneous Suite, which consists dominantly of unmetamorphosed rhyolitic and rhyodacitic volcanic rocks, with minor basalts and granitic intrusions (Fig. 1b; Torsvik et al. 2001; Gregory et al. 2009b; Wang et al. 2017, 2018).
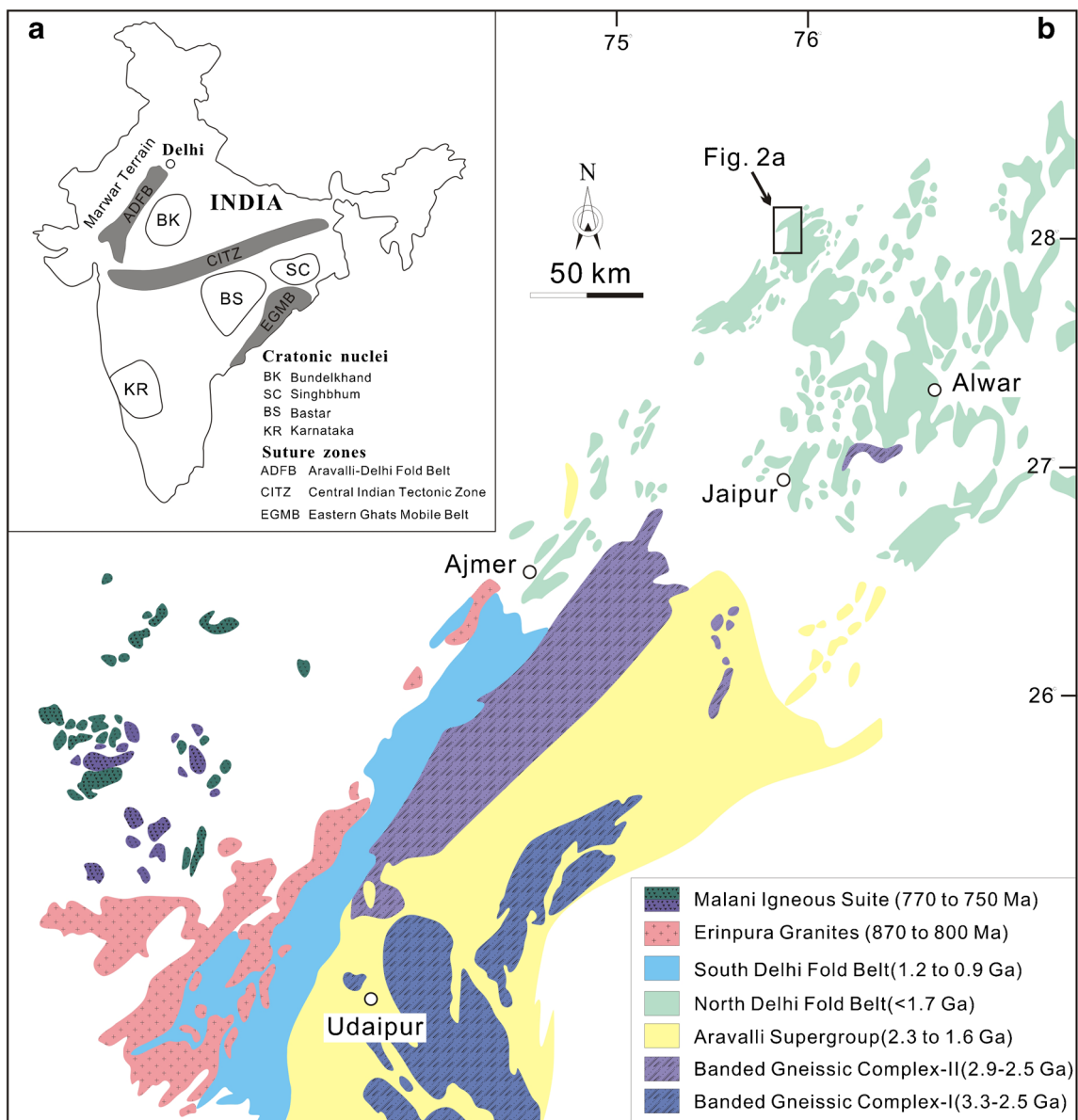
Fig. 1 a Major tectonic units of India. b A simplified geological map of the Aravalli–Delhi Fold Belt, showing major Precambrian lithotectonic units (modified from Kaur et al. 2014)

Khetri Copper Belt

The NE–SW-oriented KCB is located in the northern most part of the Aravalli–Delhi Fold Belt (Fig. 1b). Important Cu–(Au) deposits occur near the town of Khetri and include, from northeast to southwest, Banwas, Madhan-Kudhan, Kolihan, Chandmari Intervening Block, and Chandmari (Fig. 2a). The Banwas deposit is estimated to contain 30 Mt ore at 1.7 Cu and 0.3 to 3 g/t Au, the Madan-Kudan deposit 66 Mt ore at 1.12 to 1.71 wt.% Cu and 0.2 to 2 g/t Au, the Chandmari Intervening Block 12 Mt ore at 1.03 wt.% Cu, and the Kolihan and Chandmari deposits together 40 Mt ore at 1.14 to 1.62 wt.% Cu and 0.2 g/t Au (Knight et al. 2002; Bhardwaj et al. 2014).

Host rocks

The Cu–(Au) deposits in the KCB are hosted in metasedimentary rocks of the Alwar and Ajabgarh groups in the North Delhi Fold Belt (Figs. 2 and 3). The dominant host rocks include feldspathic quartzite and amphibole-bearing quartzite of the Alwar Group (Fig. 4a,b) and garnet-chlorite schist, pelitic schist, and phyllite of the Ajabgarh Group (Fig. 4c). Sedimentary structures in the Alwar and Ajabgarh groups have been interpreted to reflect shelf/shallow marine to fluvial environments (Sarkar and Dasgupta 1980). A regionally continuous, stratigraphically conformable breccia horizon occurs at the contact between the Alwar and Ajabgarh groups (Fig. 4d). The breccias are interpreted to have formed
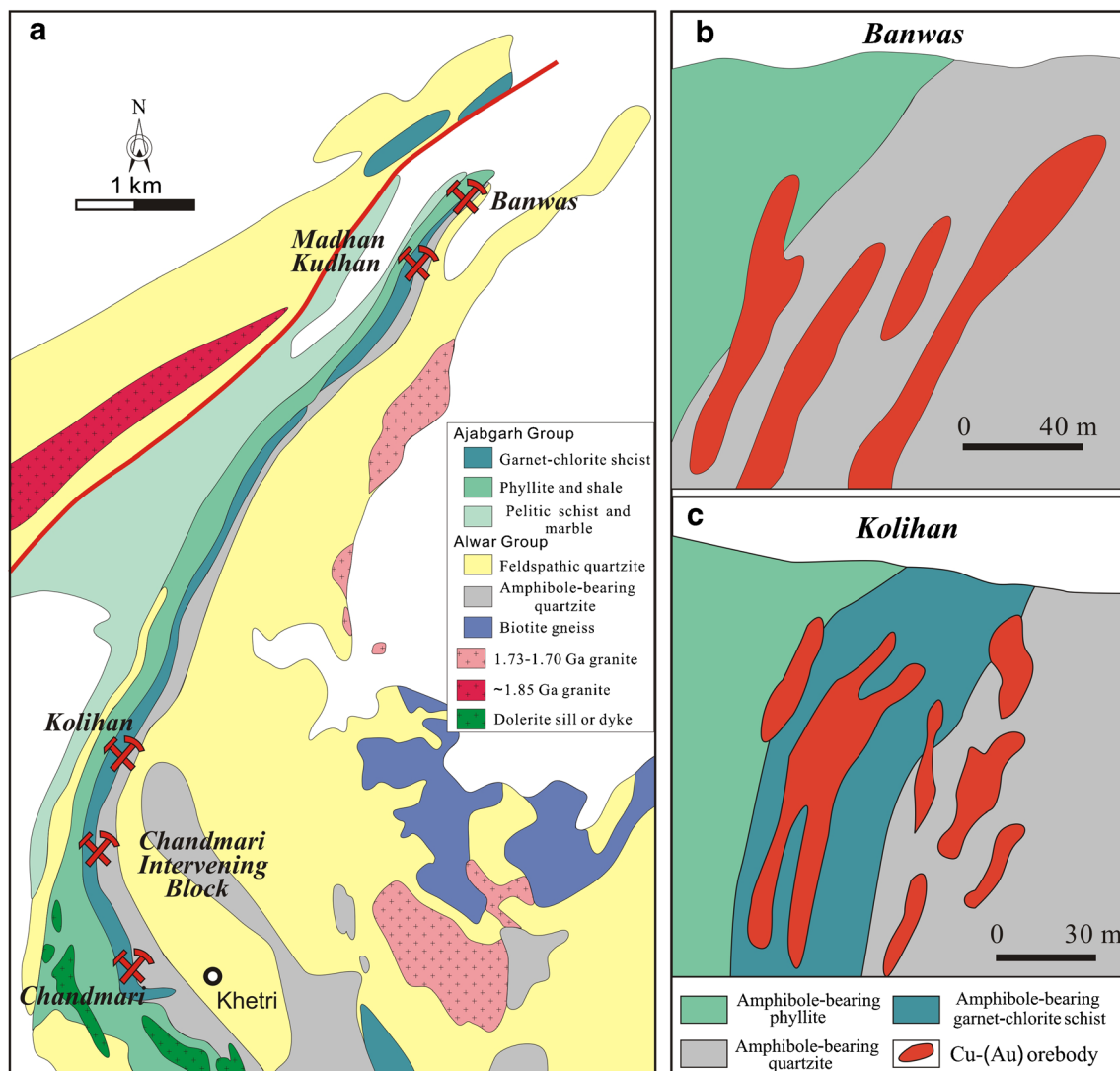
Fig. 2 **a** Simplified geological map of the Khetri Copper Belt (KCB), showing the distribution of Cu–(Au) deposits (modified after Synthetic Geological Map of the North Khetri Belt and Location of GSI-MECL Prospects (1:100,000), unpublished); **b,c** cross-sections of the Banwas and Kolihan deposits, respectively, showing the relationship between orebodies and host rocks (modified after Knight et al. 2002)

by evaporite dissolution (Knight et al. 2002). Sedimentary rocks of the Alwar and Ajabgarh groups have experienced greenschist- to amphibolite-facies metamorphism. Dates of metamorphic monazite suggest that the major metamorphic event took place at 975 to 945 Ma (Pant et al. 2008; Kaur et al. 2016). Some Paleoproterozoic granitic plutons intrude the KCB, including the ~1.82 Ga subduction-related granites and 1.73 to 1.70 Ga rift-related A-type granites (Kaur et al. 2007, 2009, 2011b; Fig. 2a). Sparse Neoproterozoic granitic intrusions were also documented adjacent to the KCB, including the 820 Ma Jhunjhunu and the 818 to 817 Ma Tosham plutons (Kaur et al. 2013).

Sedimentary rocks of the KCB show widespread calc-silicate alteration and/or albite-hematite alteration (Knight et al. 2002; Kaur et al. 2016). The calc-silicate alteration comprises assemblages of amphibole, clinopyroxene, scapolite, albite, and calcite, with subordinate epidote, apatite, titanite, and iron oxide. Albite–hematite alteration resulted in the red color of the rocks and included the formation of albite, hematite, amphibole, magnetite, and calcite. In addition to the metasedimentary rocks, the 1.73 to 1.70 Ga A-type granites were also variably altered, during which hydrothermal fluids converted plagioclase and K-feldspar into nearly pure albite (Kaur et al. 2012, 2014).

Structural setting of orebodies

The KCB has experienced early ductile and later brittle/brittle–ductile deformation (Knight et al. 2002). Rocks in the belt commonly display a sub-vertical, NE-striking foliation

Fig. 3 Geological section along the 5660 easting of the Madhan-Kudhan mine (unpublished report of the Khetri Copper Mine), showing the location of monazite-(Ce)-bearing samples
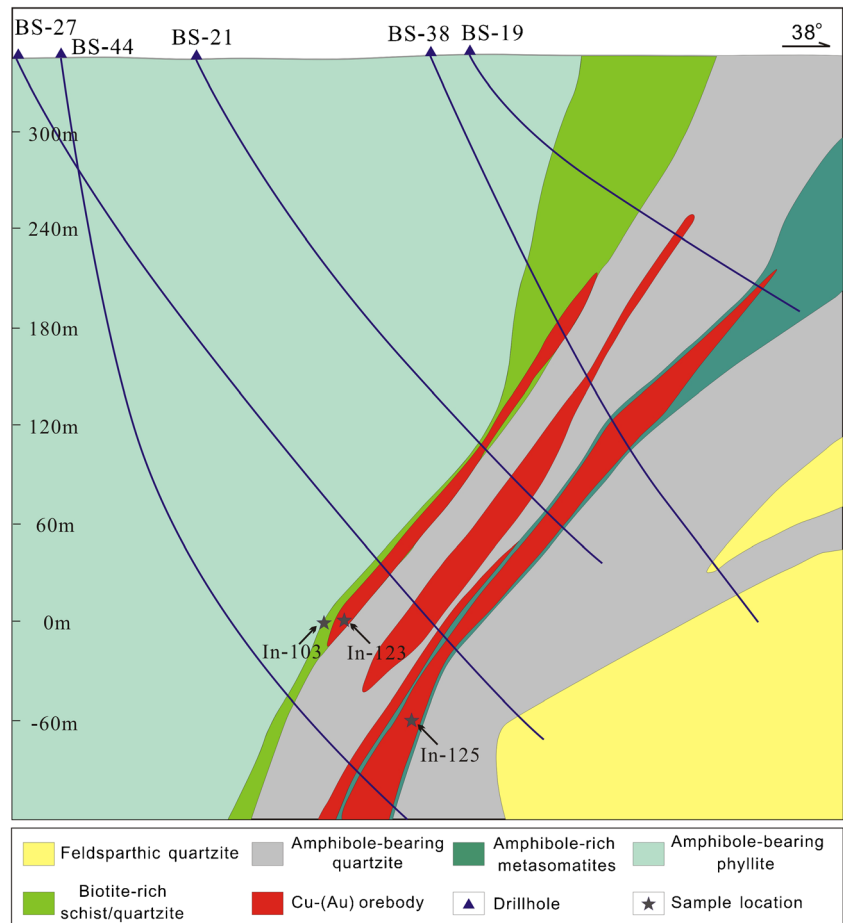
defined by peak metamorphic minerals and steeply plunging mineral lineation. Regional-scale NE-trending, doubly-plunging folds were also developed. These early structures are cut by NE- and NW-striking brittle faults and shear zones. The Cu–(Au) orebodies are located mainly along the NE-striking, west-dipping faults or shear zones, forming a series of discontinuous, sub-parallel lenses (Figs. 2b, c and 3). In some localities, the orebodies are situated at the intersection of NE- and NW-striking faults, forming subvertical cylindrically shaped bodies, or in the hinges of small-scale fault-related folds (Roy Chowdhury and Das Gupta 1965).

Alteration and mineralization

Sulfides form massive bodies, veins, and disseminations (Fig. 4e,f). The main orebodies consist of massive sulfide, whereas sulfide veins and disseminations are more abundant in the hanging wall and footwall alteration zones. Chalcopyrite and pyrrhotite are the major sulfide minerals, with subordinate pyrite and cubanite (Fig. 4e). Variable proportions of iron oxide and minor amounts of uraninite, huttonite, and REE-rich phases occur locally (Fig. 5a–c). The gangue minerals mainly include amphibole, marialitic scapolite, biotite,

chlorite, and quartz (Fig. 5b–e), with subordinate albite, tourmaline, apatite, and carbonate. Ore and gangue minerals show little evidence of deformation (Fig. 5a–e). Sulfide-bearing veins generally cross-cut the peak metamorphic fabric of the host rocks (Fig. 4f). Thus, the mineralization is interpreted to postdate the main phases of regional metamorphism and deformation.

Wallrock alteration is well-developed, mainly consisting of amphibole, biotite, chlorite, marialitic scapolite, and quartz. The amphibole alteration typically extends for hundreds of meters away from the orebodies. Amphibole occurs as randomly oriented single crystals, irregular aggregates, or preferentially oriented bands in the host rocks (Fig. 5f). Biotite, chlorite, and marialitic scapolite alterations are commonly developed tens of meters away from the orebodies. Biotite and chlorite occur generally along fractures or grain boundaries and may define the schistosity of the host rocks (Fig. 5g,h). Marialitic scapolite commonly occurs as euhedral to anhedral porphyroblasts in the host rocks. Silicification may extend for hundreds of meters away from the orebodies. Quartz occurs either as irregular aggregates overprinting the metasedimentary rocks or as veins cutting through or parallel to the foliation plane of the host rocks.

Fig. 4 Field (**a** to **d**) and sample (**e** and **h**) photographs from the KCB. **a** Quartzite of the Alwar Group. Note that the quartzite has been altered to a reddish color. **b** Banded quartzite of the Alwar Group. The dark-colored band is composed mainly of amphibole, whereas the light-colored band is composed mainly of quartz. **c** Garnet-bearing quartzite of the Ajabgarh Group. Note that garnet has been stretched and defines the gneissosity of the rock. **d** Breccia between the Alwar and Ajabgarh groups. **e** A sample of massive ore from the Madhan-Kudhan deposit, which contains chalcopyrite, pyrrhotite, Ca-group amphibole, and biotite. **f** A sulfide-bearing vein cutting the foliation plane of the host quartzite
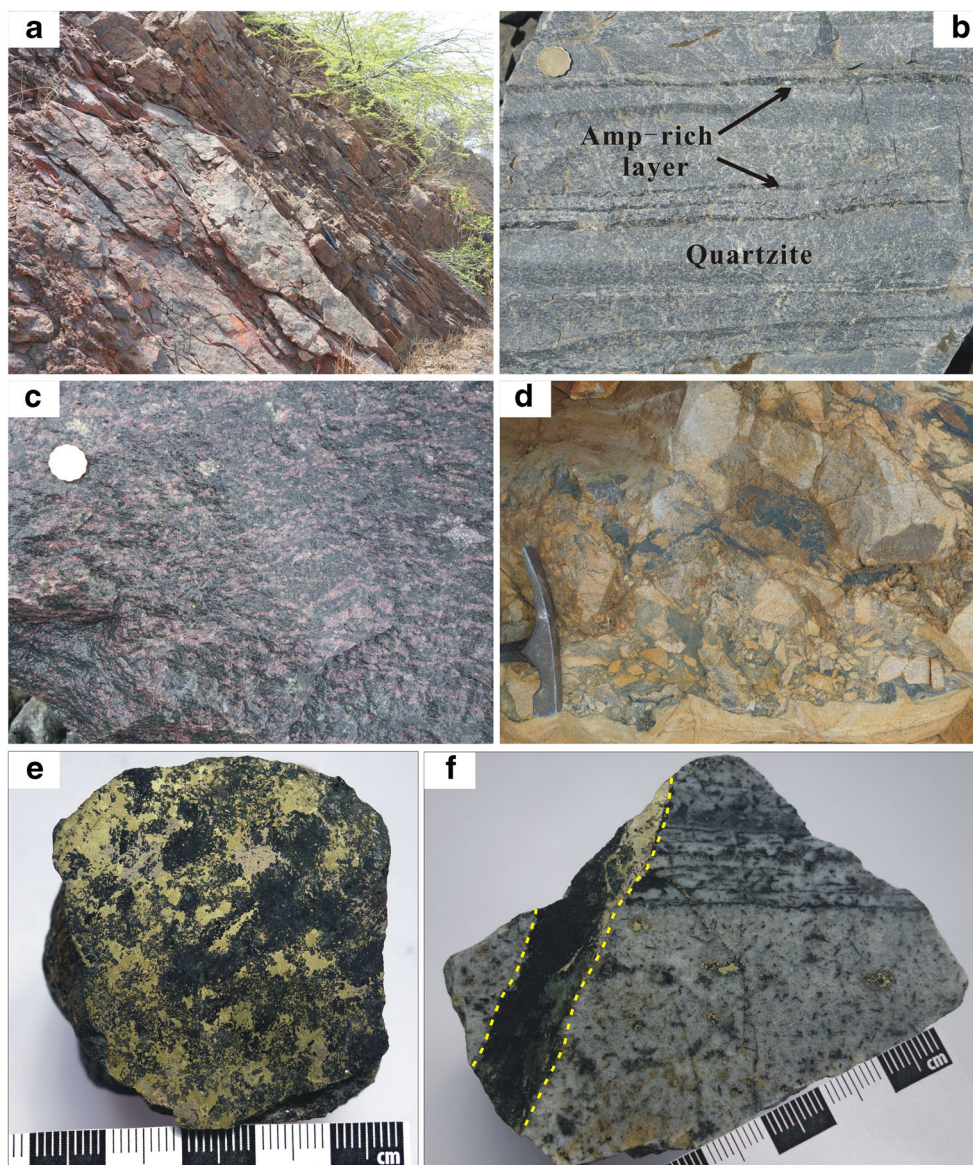
Sample description

Monazite-(Ce) crystals from four samples were studied. Three samples (In-123, In-125, and In-103) were collected from the Madhan-Kudhan mine, and one (In-192) was from the ore stock pile of the Kolihan mine. The main features of these samples are listed in Table 1.

Sample In-123 is a massive ore, where monazite-(Ce) mostly occurs in clusters with more than 10 grains in a small area (Fig. 6a). Monazite-(Ce) shows a close spatial association with chalcopyrite and biotite. Dark pleochroic halos occur at the contacts between monazite-(Ce) and biotite. Individual monazite-(Ce) crystals are euhedral to subhedral in shape and relatively uniform in size (100 to 200 μm) (Fig. 6a,b). Chalcopyrite may occur as inclusions in some monazite-(Ce) crystals (Fig. 6b).

In massive ore sample In-125, monazite-(Ce) commonly occurs as single crystals in planar to irregular contact with chalcopyrite and/or biotite and locally in contact with magnetite and zircon (Fig. 6c,d). Where monazite-(Ce) is in contact with biotite, dark pleochroic halos can be observed around the monazite-(Ce) crystals. The individual monazite-(Ce) crystals are euhedral to subhedral in shape and vary in grain size from 100 to 600 μm. Euhedral to subhedral chalcopyrite and biotite may occur as inclusions in monazite-(Ce) (Fig. 6c,d).

In-103 is a host rock that has experienced intensive biotite alteration. In this sample, monazite-(Ce) occurs as clusters in the biotite matrix (Fig. 6e). The individual cluster commonly contains more than 10 crystals in a small area. The grain size of monazite-(Ce) is highly variable in a single cluster (< 10 to > 100 μm). Dark pleochroic halos are developed at the contacts between monazite-(Ce) and

Fig. 5 Photomicrographs of ore and altered host rocks from the KCB. **a** Magnetite and chalcopyrite from a massive ore sample. The chalcopyrite is interstitial to and thus paragenetically later than the magnetite. **b** Magnetite and scapolite show close association, and they are overprinted by biotite. **c** Sulfide-allanite veins cutting cummingtonite and Ca-group amphibole. **d** Scapolite crystals replaced by chalcopyrite and biotite. **e** Sulfide–biotite–chlorite veins passing through the ore-hosting quartzite. **f** Randomly oriented cummingtonite crystals in garnet-bearing quartzite. **g** Quartzite partially replaced by biotite. **h** Quartzite partially replaced by chlorite. Abbreviations: Aln, allanite; Amp, amphibole; Bt, biotite; Ccp, chalcopyrite; Chl, chlorite; Cum, cummingtonite; Grt, garnet; Mag, magnetite; Po, pyrrhotite; Qz, quartz; Scp, scapolite
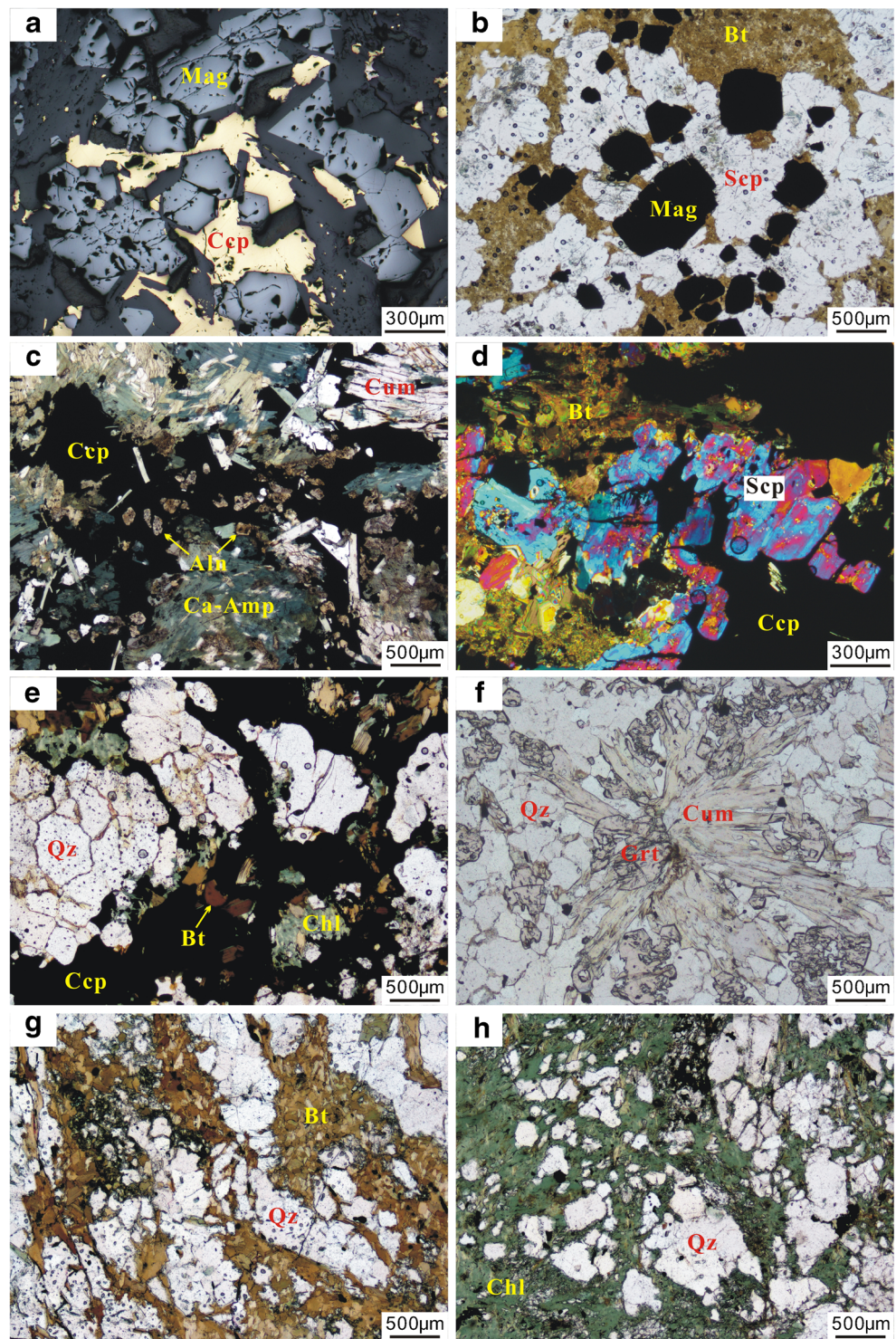
biotite. Some monazite-(Ce) crystals contain inclusions of sulfides or xenotime-(Y) (Fig. 6f).

Massive ore sample In-192 contains two types of monazite-(Ce) crystals. Type 1 crystals have planar to irregular contacts with sulfides and chlorite and usually contain inclusions of sulfides, chlorite, and/or tiny Th-rich phases

(Fig. 6g). They commonly have irregular shapes, with variable grain size (20 to 100 µm). In BSE images, they are homogeneous in color. Type 2 crystals occur as inclusions in sulfides (Fig. 6h). They are typically rounded to sub-rounded in shape and relatively uniform in size (40 to 60 µm). In contrast to type 1 crystals, type 2 crystals do not contain sulfide or

Table 1 A list of monazite-(Ce)-bearing samples in this study

Sample	Locality	Major minerals	Mineral associations	Occurrence of monazite-(Ce)
In-123	Zero meter level of the Madhan-Kudhan mine	Cummingtonite (~10 vol.%) Magnetite (~30 vol.%) Chalcopyrite and pyrrhotite (~30 vol.%) Biotite (~25 vol.%)	Late-stage sulfide minerals and biotite overprint early-stage magnetite and cummingtonite.	Monazite-(Ce) occurs as clusters in close association with sulfide minerals and biotite.
In-125	−60 m level of the Madhan-Kudhan mine	Cummingtonite (~15 vol.%) Magnetite (~20 vol.%) Tourmaline (~10 vol.%) Chalcopyrite and pyrrhotite (~30 vol.%) Biotite (~20 vol.%)	Cummingtonite occurs as the earliest phase. Later magnetite and tourmaline show close association. The latest sulfide minerals and biotite overprint cummingtonite, magnetite, and tourmaline.	Monazite-(Ce) occurs as single crystals in close association with sulfide minerals and biotite.
In-103	Zero meter level of the Madhan-Kudhan mine	Biotite (~70 vol.%) Tourmaline (~10 vol.%) Allanite and apatite (~10 vol.%) Chalcopyrite and pyrrhotite (~5 vol.%)	Tourmaline, apatite and allanite-(Ce) form relatively large, disseminated crystals in the biotite matrix. Sulfide disseminations and veinlets locally occur.	Monazite-(Ce) occurs as clusters in the biotite matrix.
In-192	Ore stock pile of the Kolihan mine	Magnetite (~30 vol.%) Chalcopyrite and pyrrhotite (~40 vol.%) Chlorite (~25 vol.%)	The early-stage magnetite occurs either as single crystals or aggregates, overprinted by later-stage sulfide minerals and chlorite	Type 1 monazite-(Ce) occurs in contact with sulfide minerals and chlorite. Type 2 monazite-(Ce) occurs as inclusions in sulfide minerals.

chlorite inclusions, but they may host quartz inclusions. In BSE image, most crystals have a continuous or discontinuous bright film near grain margins.

Analytical methods

Electron microprobe analyses

The composition of monazite-(Ce) was analyzed using a JEOL JXA-8230 electron microprobe at The University of Hong Kong. The analyses were performed using a 20 kV accelerating voltage and a 20 nA beam current. The beam spot diameter was set at 1 μm. The analyzing crystals were PET (P, U, Th, Y, Ca, and Cl), LIF (REE), LDE1 (F), and TAP (Si and Na). The K_α line was chosen for the analyses of P, Si, Ca, Na, F, and Cl, the L_α line for La, Ce, and Y, the L_β line for Pr, Nd, Sm, Eu, Gd, Tb, Dy, Ho, Er, Tm, Yb, and Lu, and the M_α line for Th and U. The counting times of peaks were 8 s for F, Cl, and Na, 30 s for P, La, Ce, Pr, and Nd, and 60 s for other elements. Background intensities were measured on both sides of the peak for half of the peak time. The standards were apatite for P, uraninite for U, huttonite for Th, hornblende for Si and Ca, monazite for La, Ce, Pr, Nd, and Sm, synthesized EuF_3 for Eu, synthesized REE metals for Gd, Tb, Dy, Ho, Er, Tm, Yb, and Y, albite for Na, topaz for F, and tugtupite for Cl. All data were corrected using standard ZAF correction

procedures. The electron microprobe analytical data are listed in Supplementary Table 1.

In situ U–Pb isotopic analyses

Monazite-(Ce) U–Pb isotopic compositions were measured using an Agilent ICP-MS, equipped with an Analyte Excite 193 nm excimer laser ablation system at the Nanjing FocuMS Analysis Lab, China. Detailed instrument operating parameters are listed in Supplementary Table 2, following Horstwood et al. (2016). The analytical procedure was similar with that described by Liu et al. (2012). The monazite-(Ce) grains were analyzed in thin sections. Analyses were performed with a spot size of 32 μm and a frequency of 4 Hz. Helium was used as the carrier gas and was mixed with argon prior to entering the ICP torch. Each spot analysis involved approximately 20 s of background data acquisition and 50 s of sample data acquisition. The external standard 44069 was used to correct for U/Pb fractionation and instrumental mass discrimination. The raw count of [204]Pb was nearly zero, so common Pb corrections were not made. The data reduction was carried out using the software package ICPMSDataCal (Liu et al. 2008). The M2 monazite was used as an external standard to monitor the accuracy of the analytical procedure. Seven spots yielded a weighted mean [206]Pb/[238]U age of 527 ± 4 Ma (2σ, MSWD = 1.01), which is consistent, within uncertainty, with the reported value of 523 ± 4 Ma (Liu et al. 2012). The U–Pb data are listed in Supplementary Table 3.

Fig. 6 Photomicrographs and BSE images of monazite-(Ce). **a** A cluster of monazite-(Ce) crystals in association with sulfides and biotite. **b** Euhedral to subhedral monazite-(Ce) crystals. Note that some sulfides occur as inclusions in monazite-(Ce). **c** A subhedral monazite-(Ce) crystal in contact with biotite and, locally, magnetite. Some subheral biotite crystals occur as inclusions in monazite-(Ce). **d** A large, euhedral monazite-(Ce) crystal in contact with chalcopyrite, biotite, quartz, and, locally, zircon. This crystal hosts some inclusions of chalcopyrite and thorite. **e** Monazite-(Ce) cluster in the biotite matrix. Note that the monazite-(Ce) crystals have highly variable sizes and shapes in individual cluster. **f** A subhedral monazite-(Ce) crystal containing an inclusion of pyrrhotite. **g** A large, irregularly shaped monazite-(Ce) crystal and several tiny monazite-(Ce) crystals in association with chlorite, pyrrhotite, and quartz. Some pyrrhotite grains and tiny Th-bearing phases occur as inclusions in the large monazite-(Ce) crystal. **h** A sub-rounded monazite-(Ce) crystal enclosed by pyrrhotite. Note that this crystal has a discontinuous bright film near the grain margin. A quartz grain occurs as inclusion in the monazite-(Ce) crystal. Abbreviation: Mnz, monazite-(Ce); Th, thorite; Zrn, zircon. Others are the same as in Fig. 5
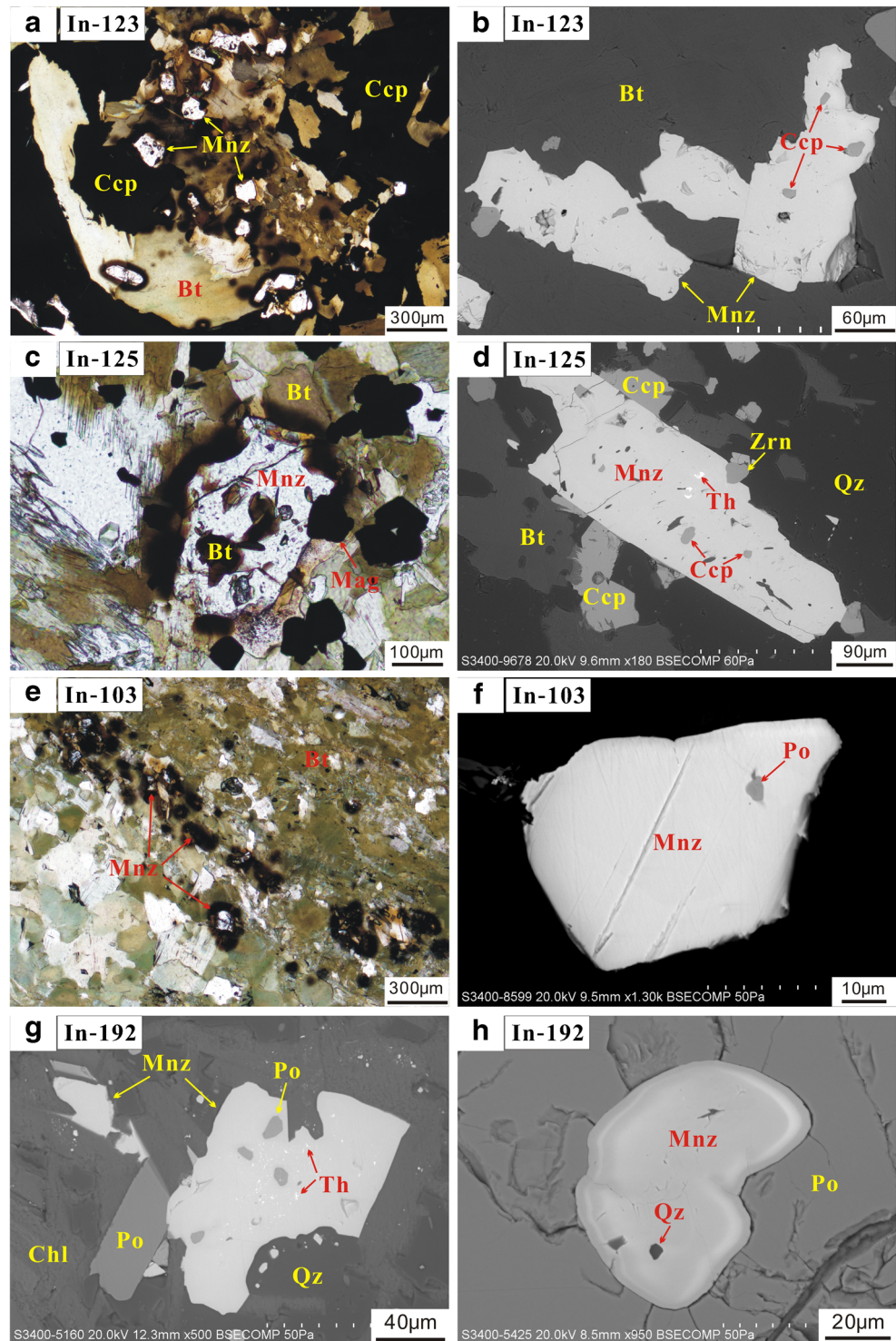
In situ Sm–Nd isotopic analyses

In situ Sm–Nd isotopic compositions of monazite-(Ce) were measured after U–Pb age determination. Monazite-(Ce) crystals from the Kolihan deposit are commonly small in size (< 50 μm), so after LA-ICP-MS U–Pb age determination, they were not suitable for Sm–Nd isotopic analyses. The analyses were performed using a Neptune multi-collector (MC) ICP-MS, equipped with a Geolas 193 nm excimer laser ablation system at the Institute of Geology and Geophysics, Chinese Academy of Sciences (IGGCAS). Detailed instrument operating parameters are listed in Supplementary Table 4, following Horstwood et al. (2016). The details of the analytical procedures were described by Liu et al. (2012). The analyses

were conducted on thin sections, with a spot size of 20 μm and a frequency of 4 Hz. Each spot analysis involved ~20 s of background data acquisition and ~40 s of sample data acquisition. After analyses of eight samples, two Namaqua monazite standards were measured for external calibration. The isobaric interference of ^{144}Sm on ^{144}Nd is significant. In order to correct for this interference, we have used the recently revised $^{147}Sm/^{149}Sm$ ratio (1.08680) and the measured $^{147}Sm/^{149}Sm$ ratio to calculate the Sm fractionation factor. Then, the measured ^{147}Sm intensity and natural $^{147}Sm/^{144}Sm$ ratio (4.866559) were used to estimate the ^{144}Sm interference on mass 144. The interference-corrected $^{146}Nd/^{144}Nd$ ratio was then normalized to 0.7219 to calculate the Nd fractionation factor. Finally, the $^{143}Nd/^{144}Nd$ and $^{145}Nd/^{144}Nd$ ratios were normalized using the exponential law. The $^{147}Sm/^{144}Nd$ ratio was calculated using the exponential law after correcting for the isobaric interference of ^{144}Sm on ^{144}Nd as described previously, and then, it was externally calibrated against the $^{147}Sm/^{144}Nd$ ratio of the Namaqua reference monazite. Monazite standard 44069 was measured to monitor the accuracy of the analytical procedure, yielding weighted mean $^{147}Sm/^{144}Nd$ and $^{143}Nd/^{144}Nd$ ratios of 0.1148 ± 0.0012 of 0.512170 ± 0.000010, respectively. These values are consistent, within uncertainty, with the reported values of 0.1159 ± 0.0064 and 0.512175 ± 0.000040, respectively (Liu et al. 2012). The in situ Sm–Nd isotopic data are listed in Supplementary Table 5.

Whole-rock Sm–Nd isotopic analyses

Whole-rock Sm–Nd isotopic compositions of four ore-hosting rocks were analyzed at IGGCAS. About 100 mg of rock powder was weighed into a 7 ml Savillex™ Teflon beaker, and the appropriate amount of mixed $^{149}Sm–^{150}Nd$ spike was added. Samples were dissolved in distilled HF + HNO_3 + $HClO_4$. Chemical separation was performed using a two-stage ion exchange procedure. Firstly, REE were isolated from the matrix elements using a standard cation exchange resin. After that, Sm and Nd were separated using Eichrom LN (LN-C-50B, 100 to 150 μm, 2 ml) chromatographic columns. The Sm–Nd isotopic measurements were conducted using an IsoProbe-T thermal ionization mass spectrometer. Mass-fractionations were corrected using $^{146}Nd/^{144}Nd$ ratio of 0.7219 and $^{147}Sm/^{149}Sm$ ratio of 1.0868. The USGS reference material BCR-2 was measured to monitor the accuracy of the analytical procedure, with the following results: 6.57 ppm Sm, 28.36 ppm Nd, and $^{143}Nd/^{144}Nd = 0.512627 \pm 11$ (2σ). These values are comparable to the reported reference values (Sm 6.547 ppm; Nd 28.26 ppm; $^{143}Nd/^{144}Nd = 0.512635 \pm 29$; Jochum et al. 2005). The Sm–Nd isotopic data are listed in Supplementary Table 6.

Analytical results

Composition of monazite-(Ce)

Eighty-five electron microprobe analytical spots were measured on sixty-two monazite-(Ce) crystals. The analyses show that monazite-(Ce) crystals from samples In-125 and In-103 and type 1 monazite-(Ce) crystals from sample In-192 are homogeneous in composition both within a single crystal and among different crystals from a single sample (Supplementary Table 1). They are rich in LREE, with Ce predominant, and are depleted in HREE. They have ThO_2 contents ranging from 0.16 to 3.42 wt.%, but mostly lower than 2.0 wt.% (Fig. 7a) and contain minor proportions of CaO (0.09 to 0.63 wt.%) and SiO_2 (<0.42 wt.%). Thus, there are minor huttonite ($ThSiO_4$) and brabantite [$CaTh(PO_4)_2$] components in these crystals.
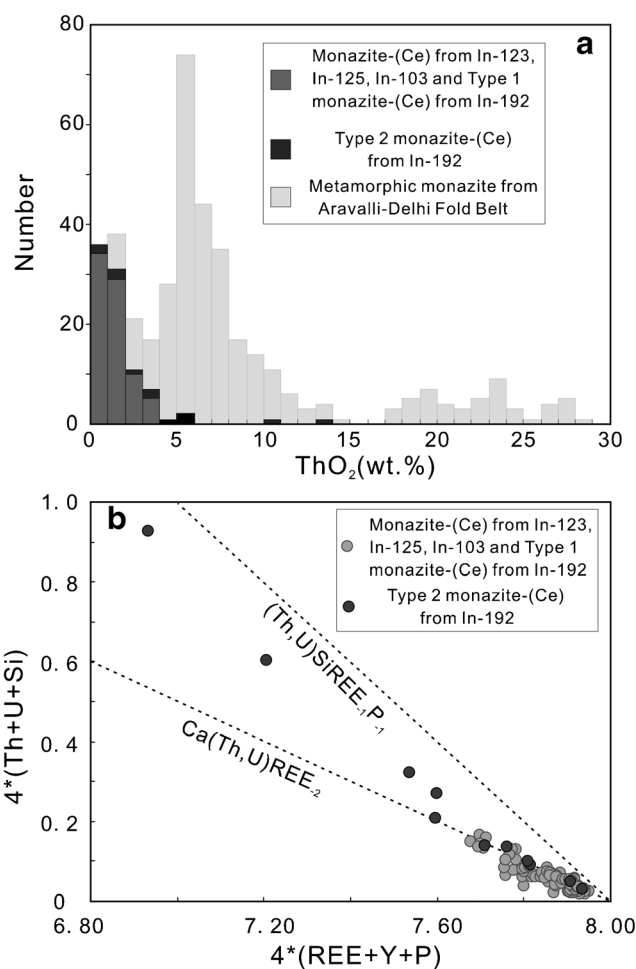
Fig. 7 **a** Histogram showing the content of ThO_2 in monazite-(Ce). The compositions of metamorphic monazite from the southern and central parts of the Aravalli–Delhi Fold Belt are also shown for comparison (Bhowmik et al. 2010; Just et al. 2011; Ozha et al. 2016). **b** Brabantite Ca(Th, U)REE_{-2} vs. huttonite (Th, U)$SiREE_{-1}P_{-1}$ exchange in monazite-(Ce) shown in the plot of 4*(Th + U + Si) vs. 4*(REE + Y + P)

Monazite-(Ce) crystals from sample In-123 are rich in LREE. Different crystals are relatively heterogeneous in LREE$_2$O$_3$, with La$_2$O$_3$ ranging from 11.27 to 19.46 wt.%, Nd$_2$O$_3$ from 10.42 to 15.77 wt.%, and Sm$_2$O$_3$ from 1.19 to 5.43 wt.% (Supplementary Table 1). Minor concentrations of ThO$_2$ (0.06 to 2.72 wt.%), CaO (0.11 to 0.63 wt.%), and SiO$_2$ (< 0.15 wt.%) were also detected.

Type 2 monazite-(Ce) crystals from sample In-192 are commonly heterogeneous in composition (Supplementary Table 1). Their P$_2$O$_5$ contents range from 26.01 to 30.71 wt.%, La$_2$O$_3$ from 12.08 to 18.10 wt.%, Ce$_2$O$_3$ from 22.33 to 28.74 wt.%, and ThO$_2$ from 0.45 to 13.59 wt.%. It is notable that there is a negative correlation between (Th + U + Si) (a.p.f.u.) and (REE + Y + P) (a.p.f.u.) (Fig. 7b), indicating that Th^{4+} is charge-balanced through the coupled substitutions of Th^{4+} + Ca^{2+} = 2(REE + Y)$^{3+}$ and Th^{4+} + Si^{4+} = P^{5+} + (REE + Y)$^{3+}$.

U–Pb age of monazite-(Ce)

Twenty-two analyses were conducted on sixteen monazite-(Ce) crystals from sample In-123 (Supplementary Table 3). The analyses show a concordant and coherent cluster on the concordia curve, with a weighted average ^{206}Pb/^{238}U age of 833 ± 5 Ma (MSWD = 3.2) (Fig. 8a).

Twenty-four analyses were conducted on fifteen monazite-(Ce) crystals from sample In-125 (Supplementary Table 3). All the analyses yield concordant ages, which form a cluster on the concordia curve with a weighted average ^{206}Pb/^{238}U age of 836 ± 7 Ma (MSWD = 3.9) (Fig. 8b).

Twenty analyses were conducted on seventeen monazite-(Ce) crystals from sample In-103 (Supplementary Table 3). Nineteen analyses yield concordant/sub-concordant results with a coherent cluster on the concordia curve,

Fig. 8 U–Pb concordia diagrams for (a) monazite-(Ce) from sample In-123, (b) monazite-(Ce) from sample In-125, (c) monazite-(Ce) from sample In-103, (d) type 1 monazite-(Ce) from sample In-192, and (e) type 2 monazite-(Ce) from sample In-192. Note that the gray ellipses in (c) and (d) were not included in the age calculation. See text for detailed explanations
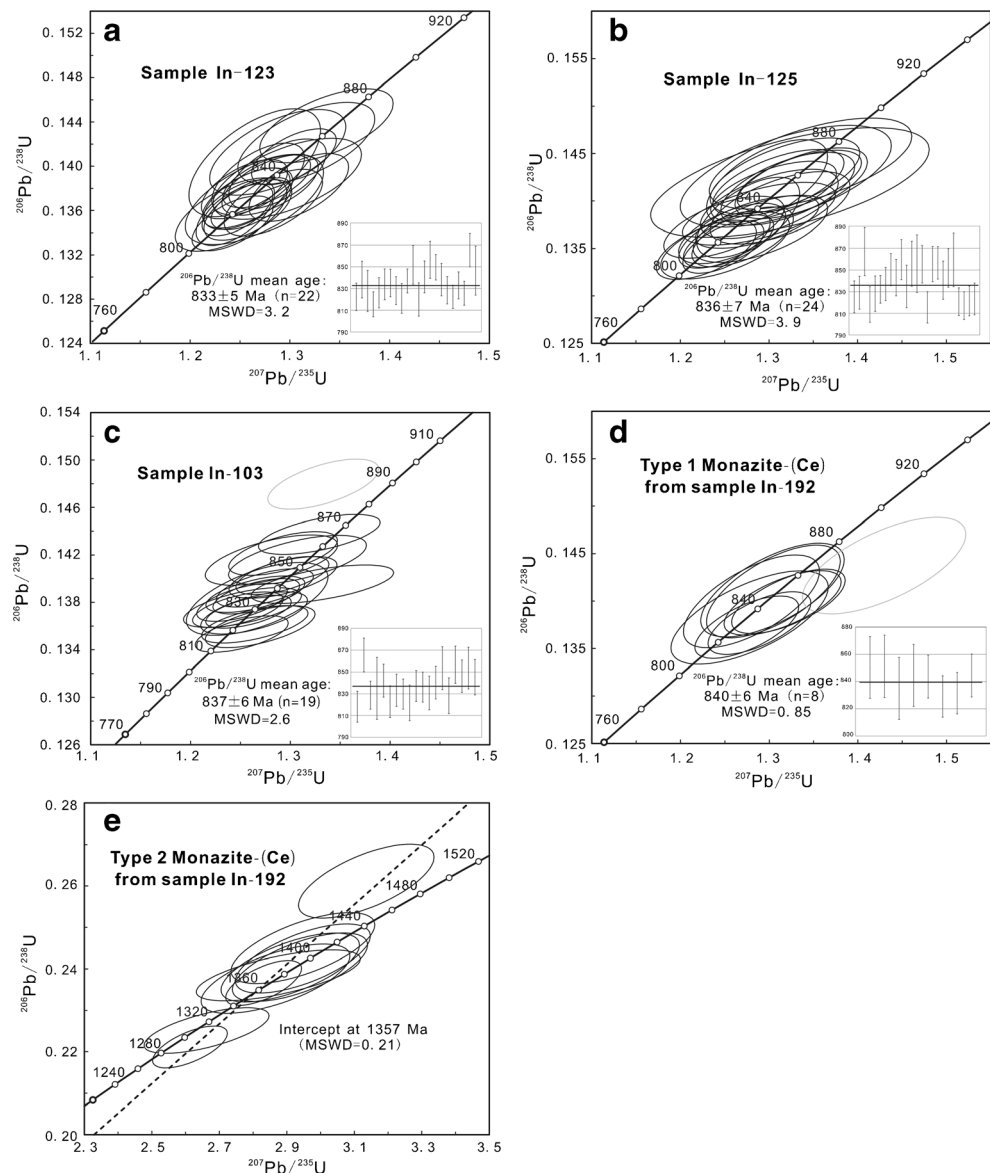
corresponding to a weighted average $^{206}Pb/^{238}U$ age of 837 ± 6 Ma (MSWD = 2.6) (Fig. 8c). One analysis (In-103-20) yields an obviously discordant age, which was not considered in the age calculation (Fig. 8c).

For sample In-192, nine spots were analyzed on nine type 1 monazite-(Ce) crystals (Supplementary Table 3). Eight concordant analyses cluster tightly on the concordia curve, yielding a weighted average $^{206}Pb/^{238}U$ age of 840 ± 6 Ma (MSWD = 0.85) (Fig. 8d). One analysis (In-192–types 1–4) was discordant and has an older $^{207}Pb/^{206}Pb$ age, which is probably caused by the existence of an old-inherited component. This analysis was excluded for age calculation. We also conducted ten analyses on ten type 2 monazite-(Ce) crystals (Supplementary Table 3). These analyses yield a wide range of apparent Pb/U ages, with $^{207}Pb/^{235}U$ ages varying from 1304 to 1441 Ma and $^{206}Pb/^{238}U$ ages from 1288 to 1496 Ma. However, the $^{207}Pb/^{206}Pb$ ages form a tight cluster, yielding a weighted average value of 1362 ± 29 Ma (MSWD = 0.21). These analyses define a regression line with a concordia intercept at 1357 Ma (MSWD = 0.21) (Fig. 8e). Such an age distribution pattern implies that different type 2 monazite-(Ce) crystals formed at approximately the same time (~ 1360 Ma) but experienced variable degrees of post-crystallization Pb-loss and/or U-loss (Williams 1998).

In situ Sm–Nd isotopic composition of monazite-(Ce)

Monazite-(Ce) crystals from sample In-103 have uniform $^{147}Sm/^{144}Nd$ (0.1117 to 0.1185) and $^{143}Nd/^{144}Nd$ (0.51132 to 0.51136) ratios. Those from sample In-125 have a moderate range of $^{147}Sm/^{144}Nd$ (0.1337 to 0.1561) and $^{143}Nd/^{144}Nd$ (0.51182 to 0.51200) ratios (Supplementary Table 5). In comparison, monazite-(Ce) crystals from sample In-123 have large ranges in $^{147}Sm/^{144}Nd$ (0.1343 to 0.1946) and $^{143}Nd/^{144}Nd$ (0.51173 to 0.51239) ratios (Supplementary Table 5). If the compositions of all the analyzed crystals are taken together, the $^{147}Sm/^{144}Nd$ ratio correlates positively with the $^{143}Nd/^{144}Nd$ ratio (Fig. 9a).

Whole-rock Sm–Nd isotopic composition of host rocks

The host metasedimentary rocks have heterogeneous present-day Sm–Nd isotopic compositions. Their $^{147}Sm/^{144}Nd$ ratios range from 0.1197 to 0.1669, and $^{143}Nd/^{144}Nd$ ratios range from 0.511415 to 0.511831 (Supplementary Table 6).

Discussion

Timing of Cu–(Au) mineralization in the KCB

The U–Pb isotopic age determinations show that type 2 monazite-(Ce) crystals from sample In-192 have significantly different ages from other monazite-(Ce) crystals. They have a
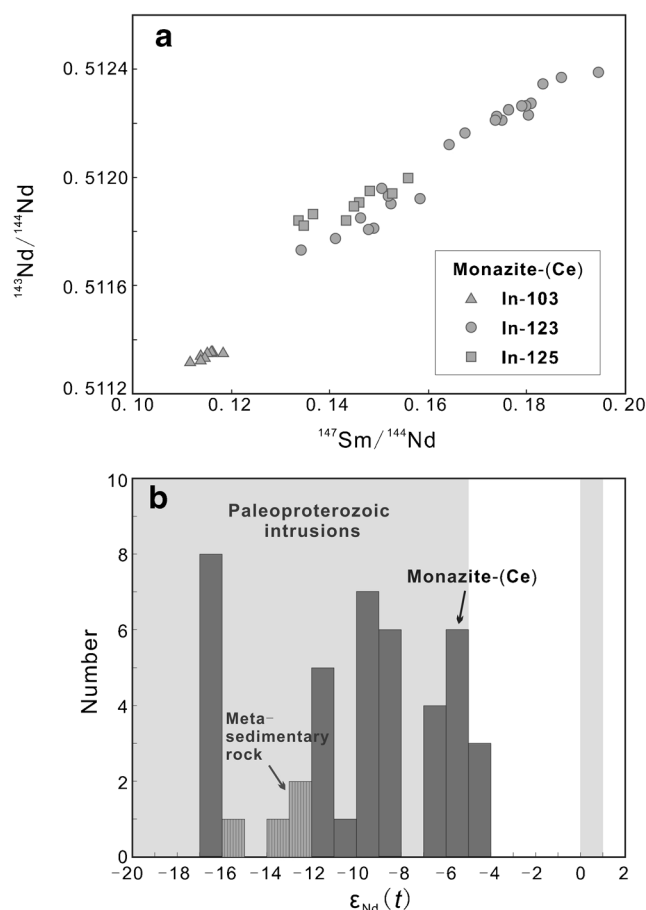
Fig. 9 **a** Plot of $^{147}Sm/^{144}Nd$ vs. $^{143}Nd/^{144}Nd$ for monazite-(Ce) from samples In-123, In-125, and In-103. **b** Histogram showing $\varepsilon_{Nd}(t = 835$ Ma) values for the monazite-(Ce). The ranges of ε_{Nd} values at 835 Ma for regional Paleoproterozoic basement intrusions (light gray areas) and ore-hosting metasedimentary rocks are also shown for comparison. The Sm–Nd isotopic data for the regional Paleoproterozoic intrusions are from Kaur et al. (2007, 2009, 2011b, 2012, 2013)

weighted average $^{207}Pb/^{206}Pb$ age of 1362 ± 29 Ma and a concordia intercept age of 1357 Ma. We note that these monazite-(Ce) crystals have a large range of ThO_2 (0.45 to 13.59 wt.%) and show concentric zoning with respect to ThO_2. Such a feature is very similar to that of metamorphic monazite, which typically contains a wide range of ThO_2 and is characterized by ThO_2 zonation (Schandl and Gorton 2004; Harlov et al. 2011; Pandey et al. 2013). Indeed, a metamorphic event at 1.4–1.3 Ga has been identified in the north and central parts of the Aravalli–Delhi Fold Belt (Hazarika et al. 2013; Ozha et al. 2016; Kaur et al. 2017a, b). We therefore propose that the type 2 monazite-(Ce) crystals in sample In-192 may be of metamorphic origin and were later incorporated into the sulfides as inclusions.

Monazite-(Ce) from samples In-123, In-125, and In-103 and type 2 monazite-(Ce) from sample In-192 have the following noteworthy features. Firstly, they occur in contact with and/or contain inclusions of sulfides, biotite, and/or chlorite (Fig. 6a–g). The mineral inclusions in monazite-(Ce) appear to

have been trapped before or during the time of monazite-(Ce) growth, with no evidence for later entrapment along healed fractures. Secondly, in some samples, monazite-(Ce) abundances are high within small areas (Fig. 6a,e), which is different from the more sparsely and homogeneously distributed magmatic or metamorphic monazite. Furthermore, most monazite-(Ce) crystals have low contents of ThO_2 (< 2.0 wt.%). All of these features fit the criteria of hydrothermal monazite as proposed by Schandl and Gorton (2004) and suggest that monazite-(Ce) grew synchronously with and/or slightly post-dated the texturally associated sulfides, biotite, and/or chlorite. It therefore follows that the U–Pb ages of these monazite-(Ce) crystals record the timing of Cu–(Au) mineralization.

Our U–Pb data show that hydrothermal monazite-(Ce) crystals from the Madhan-Kudhan and Kolihan deposits have indistinguishable U–Pb ages (833 ± 5 to 837 ± 6 and 840 ± 6 Ma, respectively), indicating that Cu–(Au) mineralization in the two deposits was broadly coeval. Considering that the other deposits in the KCB show very similar structural controls and alteration and mineralization styles with the two deposits, it is proposed that all deposits in the belt formed at ~ 835 Ma. It is notable that one hydrothermal monazite-(Ce) crystal from a metasomatically altered chlorite schist in the KCB was dated at 649 ± 40 Ma by electron microprobe analysis (Pandey et al. 2013). This age likely represents a local post-ore hydrothermal process.

Sources of REE

At the time of mineralization, the $\varepsilon_{Nd}(t = 835$ Ma) values of hydrothermal monazite-(Ce) range from − 4.3 to − 16.8, with an average value of − 9.6 (Fig. 9b). Such isotopic compositions indicate that the REE in the orebodies are predominantly of crustal origin. It is notable that the time-evolved εNd values of the regional Paleoproterozoic granitic intrusions have a very similar range with those of monazite-(Ce) at the time of mineralization (Fig. 9b). This similarity indicates that REE were likely derived from Paleoproterozoic granitic intrusions. Some hydrothermal monazite-(Ce) crystals have $\varepsilon_{Nd}(t = 835$ Ma) values similar to those of ore-hosting metasedimentary rocks (Fig. 9b), such that the regional metasedimentary rocks may also be important REE sources. An important observation is that the $\varepsilon_{Nd}(t = 835$ Ma) values of hydrothermal monazite-(Ce) are variable between, or even within, individual samples, which indicates that a range of isotopically heterogeneous materials were incorporated into the hydrothermal system.

Genetic link between Cu–(Au) mineralization and regional metasomatism

The regional Ca–Na metasomatism occurred during the Neoproterozoic, as shown by a titanite U–Pb age of 847 ± 8 Ma for a metasomatic rock containing hydrothermal albite, hematite, amphibole, calcite, and titanite (Knight et al. 2002) and a whole-rock mineral Sm–Nd isochron age of 831 ± 15 Ma for an altered mafic intrusion (Kaur et al. 2013). Our new geochronology results demonstrate that the timing of Cu–(Au) mineralization (833 to 840 Ma) falls within the age range of regional Ca–Na metasomatism (831 to 847 Ma) (Fig. 10). The temporal association between Cu–(Au) mineralization and regional metasomatism suggests a likely genetic link between them.

Fig. 10 Summary of isotopic ages for collision-related metamorphism, Neoproterozoic magmatism, regional metasomatism, and Cu–(Au) mineralization in the Aravalli–Delhi Fold Belt. Sources of the data are as follows: (1) Ozha et al. (2016); (2) Hazarika et al. (2013); (3) Bhowmik et al. (2010); (4) Pant et al. (2008); (5) Van Lente et al. (2009); (6) Just et al. (2011); (7) Singh et al. (2010); (8) Deb et al. (2001); (9) Knight et al. (2002); (10) Kaur et al. (2013); (11) this study
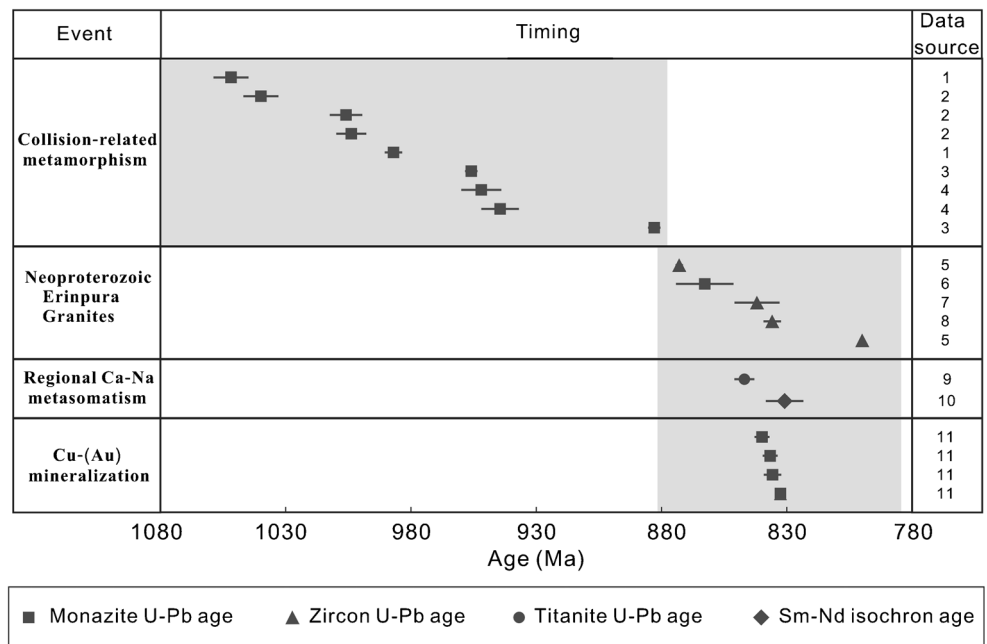
We note that marialitic scapolite extensively occurs in orebodies and ore-related alteration halos (locally up to ~20 vol.%) in the KCB. Previous studies show that at temperatures near 400 °C (approaching the average temperature of ore-forming fluids in the KCB; Knight et al. 2002), fluids containing more than 40 mol% NaCl are needed to stabilize marialitic scapolite (Vanko and Bishop 1982). Baidya et al. (2017) reported that ore-related amphibole from the Kolihan deposit contains 2.4 to 6.2 wt.% Cl. Our analyses show that ore-related biotite from the Madhan-Kudhan deposit also contains large amounts of Cl (0.4 to 5.0 wt.%). The common presence of Cl-rich amphibole and biotite is also indicative of saline ore-forming fluids. Fluids with high chlorinity are commonly interpreted to result from reaction with evaporite (Yardley 2012; Warren 2016). Thus, it is speculated that the ore-forming fluids may have circulated in upper crust and leached Cl along fluid pathways. As Cl is an effective ligand for the mobilization of metals, such as Cu, Au, and REE (Williams-Jones and Migdisov 2014), circulation of Cl-rich fluids would have led to extensive mobilization of these metals and their transport into the hydrothermal systems. Indeed, our Sm–Nd isotopic data imply that the Paleoproterozoic igneous intrusions and/or metasedimentary rocks could have contributed to the REE budget, and it is also documented that sodic metasomatism of the regional Paleoproterozoic granites was accompanied by considerable leaching of Fe, U, and REE due to the breakdown of mafic and accessory phases (Kaur et al. 2014). We note that the Cu–(Au) mineralization was temporally associated with magmatism on a regional scale (Fig. 10). It is possible that Neoproterozoic magmatism induced circulation of hydrothermal fluids in the upper crust (Kaur et al. 2014). Interaction of these fluids with meta-igneous and metasedimentary rocks would have produced widespread Ca–Na metasomatism and at the same time leached metals from the altered rocks, facilitating the formation of Cu–(Au) ore. Similar scenarios have been proposed for several iron oxide-bearing Cu–Au deposits, such as the Wernecke Breccia, Canada (Hunt et al. 2011) and those in the Carajás Mineral Province, Brazil (Xavier et al. 2008).

Conclusions

(1) The Madhan-Kudhan and Kolihan deposits from the Khetri Copper Belt, India, contain syn-ore hydrothermal monazite-(Ce). Hydrothermal monazite-(Ce) crystals have U–Pb ages of 833 ± 5 to 840 ± 6 Ma, interpreted to represent the timing of Cu–(Au) mineralization in the Khetri Copper Belt.

(2) The Kolihan deposit contains xenocrystic monazite-(Ce) crystals with an age of ~1.36 Ga. They may record a pre-ore metamorphic event in the Khetri Copper Belt.

(3) The Nd isotopic compositions suggest that REE were derived from a range of upper crustal rocks.

(4) The Cu–(Au) mineralization was coeval with regional Ca–Na metasomatism in the Khetri Copper Belt. The regional Ca–Na metasomatism was accompanied by significant mobilization of certain metals, which may facilitate the formation of Cu–(Au) ore.

References

Ahmad T, Dragusanu C, Tanaka T (2008) Provenance of Proterozoic Basal Aravalli mafic volcanic rocks from Rajasthan, Northwestern India: Nd isotopes evidence for enriched mantle reservoirs. Precambrian Res 162:150–159

Baidya AS, Paul J, Pal DC, Upadhyay D (2017) Mode of occurrences and geochemistry of amphibole in the Kolihan-Chandmari copper deposits, Rajasthan, India: insight into the ore-forming process. Ore Geol Rev 80:1092–1110

Bhardwaj R, Singh AK, Mishra VN (2014) Exploration for copper ore in Chandmari Intervening Block, Khetri Copper Belt, Rajasthan. In: 34th Annual day and national seminar, conference paper

Bhowmik SK, Bernhardt HJ, Dasgupta S (2010) Grenvillian age high-pressure upper amphibolite-granulite metamorphism in the Aravalli-Delhi mobile belt, northwestern India: new evidence from monazite chemical age and its implication. Precambrian Res 178:168–184

Buick IS, Allen C, Pandit M, Rubatto D, Hermann J (2006) The Proterozoic magmatic and metamorphic history of the Banded Gneiss Complex, central Rajasthan, India: LA-ICP-MS U–Pb zircon constraints. Precambrian Res 151:119–142

Buick IS, Clark C, Rubatto D, Hermann J, Pandit M, Hand M (2010) Constraints on the Proterozoic evolution of the Aravalli-Delhi Orogenic belt (NW India) from monazite geochronology and mineral trace element geochemistry. Lithos 120:511–528

Chiaradia M, Schaltegger U, Spikings R, Wotzlaw JF, Ovtcharova M (2013) How accurately can we date the duration of magmatic-hydrothermal events in porphyry systems?—An invited paper. Econ Geol 108:565–584

Das Gupta SP (1974) Geological setting and origin of sulphide deposits in the Khetri copper belt, Rajasthan. Bull Geol Min Metall Soc India 47:221–238

Davis DW, Schandl ES, Wasteneys HA (1994) U–Pb dating of alteration around massive sulfide deposits in the Superior province, Canada. Contrib Mineral Petrol 115:427–437

Deb M, Thorpe RI, Kristic D, Corfu F, Davis DW (2001) Zircon U–Pb and galena Pb isotope evidence for an approximate 1.0 Ga terrane

constituting the western margin of the Aravalli-Delhi orogenic belt, northwestern India. Precambrian Res 108:195–213

Dharma Rao CV, Santosh M, Purohit R, Wang J, Jiang X, Kusky T (2011) LA-ICP-MS U-Pb zircon age constraints on the Paleoproterozoic and Neoarchean history of the Sandmata Complex in Rajasthan within the NW Indian Plate. J Asian Earth Sci 42:286–305

Fisher CM, McFarlane CRM, Hanchar JM, Schmitz MD, Sylvester PJ, Lam R, Longerich HP (2011) Sm-Nd isotope systematics by laser ablation-multicollector-inductively coupled plasma mass spectrometry: methods and potential natural and synthetic reference materials. Chem Geol 284:1–20

Fisher CM, Hanchar JM, Miller CF, Phillips S, Vervoort J, Whitehouse MJ (2017) Combining Nd isotopes in monazite and Hf isotopes in zircon to understand complex open-system processes in granitic magmas. Geology 45(4):267–270

Goudie DJ, Fisher CM, Hanchar JM, Crowley JL, Ayers JC (2014) Simultaneous in situ determination of U-Pb and Sm-Nd isotopes in monazite by laser ablation ICP-MS. Geochem Geophys Geosyst 15:2575–2600

Gregory CJ, McFarlane CRM, Hermann J, Rubatto D (2009a) Tracing the evolution of calcalkaline magmas: in-situ Sm-Nd isotope studies of accessory minerals in the Bergell Igneous Complex, Italy. Chem Geol 260:73–86

Gregory LC, Meert JG, Bingen B, Pandit MK, Torsvik TH (2009b) Paleomagnetism and geochronology of the Malani Igneous Suite, Northwest India: implications for the configuration of Rodinia and the assembly of Gondwana. Precambrian Res 170:13–26

Gupta P, Guha DB, Chattopadhyay B (1998) Basement-cover relationship in the Khetri Copper Belt and the emplacement mechanism of the granite massifs, Rajasthan. J Geol Soc India 52:417–432

Harlov DE, Wirth R, Hetherington CJ (2011) Fluid-mediated partial alteration in monazite: the role of coupled dissolution-reprecipitation in element redistribution and mass transfer. Contrib Mineral Petrol 162:329–348

Hazarika P, Upadhyay D, Mishra B (2013) Contrasting geochronological evolution of the Rajpura-Dariba and Rampura-Agucha metamorphosed Zn-Pb deposit, Aravalli-Delhi Belt, India. J Asian Earth Sci 73:429–439

Heron AM (1953) The geology of Central Rajputana: Mem Geol Surv India 79, 339 pp

Horstwood MSA, Kosler J, Gehrels G, Jackson SE, McLean NM, Paton C, Pearson NJ, Sircombe K, Sylvester P, Vermeesch P, Bowring JF, Condon DJ, Schoene B (2016) Community-derived standards for LA-ICP-MS U-(Th-)Pb geochronology—uncertainty propagation, age interpretation and data reporting. Geostand Geoanal Res 40: 311–332

Hunt JA, Baker T, Cleverley J, Davidson GJ, Fallick AE, Thorkelson DJ (2011) Fluid inclusion and stable isotope constraints on the origin of Wernecke Breccia and associated iron oxide-copper-gold mineralization, Yukon. Can J Earth Sci 48:1425–1445

Jochum KP, Nohl U, Herwig K, Lammel E, Stoll B, Hofmann AW (2005) GeoReM: a new geochemical database for reference materials and isotopic standards. Geostand Geoanal Res 29:333–338

Just J, Schulz B, de Wall H, Jourdan F, Pandit MK (2011) Monazite CHIME/EPMA dating of Drinpura granitoid deformation: implications for Neoproterozoic tectono-thermal evolution of NW India. Gondwana Res 19:402–412

Kaur P, Chaudhri N, Raczek I, Kröner A, Hofmann AW (2007) Geochemistry, zircon ages and whole-rock Nd isotopic systematics for Palaeoproterozoic A-type granitoids in the northern part of the Delhi belt, Rajasthan, NW India: implications for late Palaeoproterozoic crustal evolution of the Aravalli craton. Geol Mag 144:361–378

Kaur P, Chaudhri N, Raczek I, Kröner A, Hofmann AW (2009) Record of 1.82 Ga Andean-type continental arc magmatism in NE Rajasthan, India: insights from zircon and Sm-Nd ages, combined with Nd-Sr isotope geochemistry. Gondwana Res 16:56–71

Kaur P, Zeh A, Chaudhri N, Gerdes A, Okrusch M (2011a) Archaean to Palaeoproterozoic crustal evolution of the Aravalli orogen, NW India, and its hinterland: the U-Pb and Hf isotope record of detrital zircon. Precambrian Res 187:155–164

Kaur P, Chaudhri N, Raczek I, Kröner A, Hofmann AW, Okrusch M (2011b) Zircon ages of late Palaeoproterozoic (ca. 1.72–1.70 Ga) extension-related granitoids in NE Rajasthan, India: regional and tectonic significance. Gondwana Res 19:1040–1053

Kaur P, Chaudhri N, Hofmann AW, Raczek I, Okrusch M, Skora S, Baumgartner LP (2012) Two-stage, extreme albitization of A-type granites from Rajasthan, NW India. J Petrol 53:919–948

Kaur P, Chaudhri N, Hofmann AW, Raczek I, Okrusch M (2013) Geochemistry and Sm-Nd geochronology of the metasomatised mafic rocks in the Khetri complex, Rajasthan, NW India: evidence of an Early Cryogenian metasomatic event in the northern Aravalli orogen. J Asian Earth Sci 62:401–413

Kaur P, Chaudhri N, Hofmann AW, Raczek I, Okrusch M, Skora S, Koepke J (2014) Metasomatism of ferroan granites in the northern Aravalli orogen, NW India: geochemical and isotopic constraints, and its metallogenic significance. Int J Earth Sci 103:1083–1112

Kaur P, Zeh A, Okrusch M, Chaudhri N, Gerdes A, Bratz H (2016) Separating regional metamorphic and metasomatic assemblages and events in the northern Khetri complex, NW India: evidence from mineralogy, whole-rock geochemistry and U-Pb monazite chronology. J Asian Earth Sci 129:117–141

Kaur P, Zeh A, Chaudhri N (2017a) Palaeoproterozoic continental-arc magmatism, and Neoproterozoic metamorphism in the Aravalli-Delhi orogenic belt, NW India: new constraints from in situ zircon U-Pb-Hf isotope systematics, monazite U-Pb dating and whole-rock geochemistry. J Asian Earth Sci 136:68–88

Kaur P, Zeh A, Chaudhri N, Eliyas N (2017b) Two distinct sources of 1.73–1.70 Ga A-type granites from the northern Aravalli orogen, NW India: constraints from in situ zircon U-Pb ages and Lu-Hf isotopes. Gondwana Res 49:164–181

Kempe U, Lehmann B, Wolf D, Rodionov N, Bombach K, Schwengfelder U, Dietrich A (2008) U-Pb SHRIMP geochronology of Th-poor, hydrothermal monazite: an example from the Llallagua tin-porphyry deposit, Bolivia. Geochim Cosmochim Acta 72:4352–4366

Knight J, Lowe J, Joy S, Cameron J, Merrillees J, Nag S, Shah N, Dua G, Jhala K (2002) The Khetri Copper Belt, Rajasthan: iron oxide copper-gold terrane in the Proterozoic of NW India, in Porter, T.M., e.d., Hydrothermal iron oxide copper–gold & related deposits: a global perspective, volume 2: Adelaide, PGC Publishing, 321–341

Li XC, Zhou MF, Chen WT, Zhao XF, Tran MD (2018) Uranium-lead dating of hydrothermal zircon and monazite from the Sin Quyen Fe-Cu-REE-Au-(U) deposit, northwestern Vietnam. Mineral Deposita 53:399–416

Liu YS, Hu ZC, Gao S, Günther D, Xu J, Gao CG, Chen HH (2008) In situ analysis of major and trace elements of anhydrous minerals by LA-ICP-MS without applying an internal standard. Chem Geol 257: 34-43

Liu ZC, Wu FY, Yang YH, Yang JH, Wilde SA (2012) Neodymium isotopic compositions of the standard monazites used in U-Th-Pb geochronology. Chem Geol 334:221–239

McKenzie NR, Hughes NC, Myrow PM, Banerjee DM, Deb M, Planavsky NJ (2013) New age constraints for the Proterozoic Aravalli-Delhi successions of India and their implications. Precambrian Res 238:120–128

Ozha MK, Mishra B, Hazarika P, Jeyagopal AV, Yadav GS (2016) EPMA monazite geochronology of the basement and supracrustal rocks within PurBanera basin, Rajasthan: evidence of Columbia breakup in northwestern India. J Asian Earth Sci 117:284–303

Pandey M, Pant NC, Kumar S (2013) Criteria to distinguish between regional and contact zone monazite—a case study from Proterozoic North Delhi Fold Belt (NDFB), India. Episodes 36: 275–289

Pandit MK, Carter LM, Ashwal LD, Tucker RD, Torsvik TH, Jamtveit B, Bhushan SK (2003) Age, petrogenesis and significance of 1 Ga granitoids and related rocks from the Sendra area, Aravalli Craton, NW India. J Asian Earth Sci 22:363–381

Pandit MK, Wall H, Daxberger H, Just J, Bestmann M, Sharma KK (2011) Mafic rocks from Erinpura gneiss terrane in the Sirohi region: possible ocean-floor remnants in the foreland of the Delhi Fold Belt, NW India. J Earth Syst Sci 120:627–641

Pandur K, Ansdell KM, Kontak DJ, Halpin KM, Creighton S (2016) Petrographic and mineral chemical characteristics of the Hoidas Lake Deposit, Northern Saskatchewan, Canada: constraints on the origin of a distal magmatic-hydrothermal REE system. Econ Geol 111:667–694

Pant NC, Kundu A, Joshi S (2008) Age of metamorphism of Delhi Supergroup rocks—electron microprobe ages from Mahendragarh district, Haryana. J Geol Soc India 72:365–372

Rasmussen B, Sheppard S, Fletcher IR (2006) Testing ore deposit models using in situ U-Pb geochronology of hydrothermal monazite: Paleoproterozoic gold mineralization in northern Australia. Geology 34:77–80

Roy Chowdhury MK, Das Gupta SP (1965) Ore-localization in the Khetri Copper Belt, Rajasthan, India. Econ Geol 60:69–88

Roy AB, Kröner A (1996) Single zircon evaporation ages constraining the growth of the Archaean Aravalli craton, northwestern Indian shield. Geol Mag 133:333–342

Roy AB, Kröner A, Bhattacharya PK, Rathore S (2005) Metamorphic evolution and zircon geochronology of early Proterozoic granulites in the Aravalli Mountains of northwestern India. Geol Mag 142: 287–302

Roy AB, Kröner A, Rathore S, Laul V, Purohit R (2012) Tectono-metamorphic and geochronologic studies from Sandmata Complex, northwest Indian Shield: implications on exhumation of Late-Palaeoproterozoic granulites in an Archaean-early Palaeoproterozoic granite-gneiss terrane. J Geol Soc India 79:323–334

Sarkar SC, Dasgupta S (1980) Geologic setting, genesis and transformation of the sulfide deposits in the northern part of the Khetri copper belt, Rajasthan, India—an outline. Mineral Deposita 15:117–137

Schandl ES, Gorton MP (2004) A textural and geochemical guide to the identification of hydrothermal monazite: criteria for selection for samples for dating epigenetic hydrothermal ore deposits. Econ Geol 99:1027–1035

Singh YK, De Waele B, Karmarkar S, Sarkar S, Biswal TK (2010) Tectonic setting of the Balaream-Kui-Surpagla-Kengora granulites of the South Delhi Terrane of the Aravalli Mobile Belt, NW India and its implication on correlation with the East African Orogen in the Gondwana assembly. Precambrian Res 183:669–688

Sinha-Roy S, Malhotra G, Mohanty M (1998) Geology of Rajasthan. Geological Society of India, Bangalore, p 278

Torsvik TH, Carter LM, Ashwal LD, Bhushan SK, Pandit MK, Jamtveit B (2001) Rodinia refined or obscured: palaeomagnetism of the Malani Igneous Suite (NW India). Precambrian Res 108:319–333

Van Lente B, Ashwal LD, Pandit MK, Bowring SA, Torsvik TH (2009) Neoproterozoic hydrothermally altered basaltic rocks from Rajasthan, northwest India: implications for late Precambrian tectonic evolution of the Aravalli Craton. Precambrian Res 170:202–222

Vanko DA, Bishop FC (1982) Occurrence and origin of marialitic scapolite in the Humboldt lopolith, N.W. Nevada. Contrib Mineral Petrol 81:277–289

Vijaya Rao V, Rajendra Prasad B, Reddy PR, Tewari HC (2000) Evolution of Proterozoic Aravalli Delhi Fold Belt in northwestern Indian Shield from seismic studies. Tectonophysics 327:109–130

Wang W, Cawood PA, Zhou MF, Pandit MK, Xia XP, Zhao JH (2017) Low-δ^{18}O rhyolites from the Malani Igneous Suite: a positive test for South China and NW India linkage in Rodinia. Geophys Res Lett 44:10298–10305

Wang W, Pandit MK, Zhao JH, Chen WT, Zheng JP (2018) Slab break-off triggered lithosphere-asthenosphere interaction at a convergent margin: the Neoproterozoic bimodal magmatism in NW India. Lithos 296-299:281–296

Warren JK (2016) Magma-evaporite-hydrothermal metal associations, in Warren, J.K., e.d., Evaporites, Second edition: Springer Berlin, p. 1591–1656

Wiedenbeck M, Goswami JN (1994) An ion-probe single zircon Pb age from the Mewar Gneiss at Jhamarkotra, Rajasthan. Geochim Cosmochim Acta 58:2135–2141

Wiedenbeck M, Goswami JN, Roy AB (1996) Stabilisation of the Aravalli craton of the north-western India at 2.5 Ga: an ion-microprobe zircon study. Chem Geol 129:325–340

Williams IS (1998) U-Th-Pb geochronology by ion microprobe. Rev Econ Geol 7:1–35

Williams ML, Jercinovic MJ, Hetherington CJ (2007) Microprobe monazite geochronology: understanding geologic processes by integrating composition and chronology. Annu Rev Earth Planet Sci 35: 137–175

Williams-Jones AE, Migdisov AA (2014) Experimental constraints on the transport and deposition of metals in ore-forming hydrothermal systems, vol 18. Society of Economic Geologists, Inc. Special Publication, pp 77–95

Xavier RP, Wiedenbeck M, Trumbull RB, Dreher AM, Monteiro LVS, Rhede D, Araújo CEG, Torresi I (2008) Tourmaline B-isotopes fingerprint marine evaporites as the source of high-salinity ore fluids in iron oxide-copper-gold deposits, Carajás Mineral province (Brazil). Geology 36:743–746

Yardley BWD (2012) The chemical composition of metasomatic fluids in the crust, in Harlov, D.E., and Austrheim H., e.d., Metasomatism and the chemical transformation of rock, Springer Berlin, p. 17–53